Materials Today Communications 38 (2024) 108408

Contents lists available at ScienceDirect

Materials Today Communications

journal homepage: www.elsevier.com/locate/mtcomm

Effects of different Cr contents on microstructure, mechanical and electrical properties of Cu-Zr-Cr alloy

Zheng'ao Li [a], Meng Zhou [a,b,c,*], Ke Jing [a], Yong Liu [a,b,c], Gang'ao Xin [a], Haoyan Hu [a], Jin Zou [d], Baohong Tian [a,b,c], Yi Zhang [a,b,c,*], Xu Li [e], Alex A. Volinsky [f]

[a] Henan University of Science and Technology, School of Materials Science and Engineering, Luoyang 471023, PR China
[b] Provincial and Ministerial Co-construction of Collaborative Innovation Center for Non-ferrous Metals New Materials and Advanced Processing Technology, Henan Province, Luoyang 471023, PR China
[c] Henan Province Key Laboratory of Nonferrous Materials Science and Processing Technology, Luoyang 471023, PR China
[d] Jiangxi Key Laboratory for Advanced Copper and Tungsten Materials, Jiangxi Academic of Sciences, Nanchang 330096, PR China
[e] Center for Advanced Measurement Science, National Institute of Metrology, Beijing 100029, PR China
[f] Department of Mechanical Engineering, University of South Florida, 4202 E. Fowler Ave. ENG 030, Tampa 33620, USA

ARTICLE INFO

Keywords:
Cu alloys
Properties
Microstructure
EBSD
Strengthening and conductivity mechanisms

ABSTRACT

Cu-0.3Zr-0.05Cr and Cu-0.3Zr-0.15Cr alloys were prepared by vacuum melting method, and solution treatment was carried out at 900 °C. In order to explore the best heat treatment process, the alloy was aged with different parameters. Through performance test and microstructure analysis, the following conclusions were drawn. After hot forging, 60% cold rolling, and 450 °C 120 min aging treatment, Cu-0.3Zr-0.15Cr alloy exhibited favorable performance with 180 HV hardness, 467 MPa tensile strength, 84.4% IACS electrical conductivity, and 12.1% elongation. The Cu-0.3Zr-Cr alloys showed a considerable increase in texture content and maximum texture strength as the Cr concentration rose. The primary mechanism for strengthening alloys is precipitation strengthening. During the aging treatment, Cr and Cu_5Zr phases are precipitated in the alloy. The Cr phase formed a semi-coherent interface with the Cu matrix, which allowed the alloy to retain its good flexibility. The dispersed precipitates greatly increased the strength and electrical conductivity of the alloy, resulting in outstanding overall performance.

1. Introduction

Copper alloys exhibit superior mechanical qualities and good electrical conductivity [1–3]. They are extensively utilized in many different industrial sectors, including electronics, transportation, and manufacturing [4,5]. Cu-Cr alloy, a popular precipitation-strengthened copper alloy, is ideal for usage as a material for integrated circuit lead frames and high-speed contact wires because of its enough strength and electrical conductivity [6–10]. But the Cr phase is more prone to aggregation and development during the aging process, which causes over-aging and reduced strength. Studies have demonstrated that Zr can improve the Cr phase's quality and speed up its transition to the spherical phase. Additionally, Zr can generate a Zr-rich precipitation phase at grain boundaries, improving the creep and fatigue strength, mid-temperature brittleness, and grain boundaries' strength significantly [11]. Cu-Cr alloy performance is greatly enhanced by this, enabling Cu-Cr-Zr alloy to have high strength and outstanding electrical conductivity. Ma et al. [12] used Cu-0.4Cr-0.03Zr in a hot forged state and after a secondary cold rolling aging treatment. With an electrical conductivity of over 90% IACS, 9% elongation, and a strength at yield of over 600 MPa, the alloy included a high density of common-lattice or semi-common-lattice nano-precipitated phases. The link between the microstructure and characteristics of the Cu-0.98% Cr-0.057% Zr alloy was investigated by Fu et al. [13]. At room temperature, the elongation reduces as rolling deformation increases. This is mostly because the ductile Goss and Brass textures change into copper textures with low toughness. This demonstrates that there is a considerable association between the alloy's ductility and textural change. In their study of Cu-0.1Cr-0.1Zr and Cu-0.9Cr-0.1Zr alloys, Bodyakova et al. [14] discovered that the microstructure of the Cu-0.1Cr-0.1Zr alloy in its peak-aged state is characterized by a diffuse distribution of larger Particles of Cr observing 8–10 nm, which gives rise to the corresponding

* Corresponding authors at: Henan University of Science and Technology, School of Materials Science and Engineering, Luoyang 471023, PR China.
E-mail addresses: zhoumeng0902@126.com (M. Zhou), zhshgu436@163.com (Y. Zhang).

https://doi.org/10.1016/j.mtcomm.2024.108408
Received 4 December 2023; Received in revised form 26 January 2024; Accepted 16 February 2024
Available online 17 February 2024

Orowan strengthening mechanism, whereas the presence of tiny 3–4.5 nm sheared Cr particles is primarily responsible for the strengthening of the Cu-0.9Cr-0.1Zr alloy under peak-aging conditions. The Nishiyama-Wasserman orientation relationship and the homogenous dispersion of small 3–4.5 nm sheared Cr-rich particles are primarily responsible for the strengthening of the Cu-0.9Cr-0.1Zr alloy under peak-aging conditions. Many scholars have tried to change the Cu-Cr-Zr alloy microstructure to improve its comprehensive performance. They used equal channel angular pressing and high-pressure torsion to strengthen the alloy's structure. In addition, multi-directional forging can efficiently produce copper with ultrafine grain structure at room and moderate temperatures, thereby improving the initial performance of the alloy [15–19].

While the researchers have studied Cu-Cr alloys with trace additions of Zr (<0.2 wt%) in great detail, there are fewer studies of the Cu-Zr-Cr alloys with Zr as the main additive element and Cr as a secondary additive [12–14]. Thus, in order to achieve superior microstructure, hot-forged Cu-0.3Zr-0.05Cr and Cu-0.3Zr-0.15Cr alloys were chosen for aging treatment following 60% cold rolling in this research. By using EBSD and TEM to examine the alloy's microstructure and study its texture evolution, the strengthening and conductive mechanism of the alloy was discovered. The results helped to clarify how the cold rolling and aging processes affected the alloy's characteristics.

2. Experimental materials and procedures

An electrolytic copper cathode, Cu-10% Zr, and Cu-10% Cr intermediate alloys were used as raw materials to manufacture the Cu-0.3Zr-0.05Cr and Cu-0.3Zr-0.15Cr alloys. The alloys were melted in a ZG-5Kg vacuum induction creating furnace. Table 1. lists each alloy's exact composition. To get the greatest benefit possible microstructure, the ingot underwent hot forging treatment. In a box furnace, the alloy ingot (measuring φ100 mm by × 120 mm) was first heated to 850 °C and then kept there for a single hour. Next, a C41–750 air hammer was used to hot forge it into a φ40 mm × 230 mm bar. From there, sheets measuring 100 mm × 10 mm × 2 mm were cut. In order to determine the optimal solution process, experiments were carried out at different temperatures and holding times. The results show that the solution is better at 900 °C for 1 hour and has the advantage of low cost.

In an OTF-1200X tube furnace, the samples were heated to 900 °C for 60 minutes, and then they were quickly cooled to room temperature. After that, the alloys were cold rolled by 60% using an MSK-5070-AC roll mill. Finally, the samples were placed into a tube furnace for aging treatment at 400–550 °C for 0–360 min with high-purity argon gas purged.

A HVS-1000 hardness tester, a HY-SYJ20 universal tensile testing equipment, and a Sigma 2008B digital eddy current metal electrical conductivity meter were used to test the alloys' characteristics. Each sample's electrical conductivity and hardness were tested five times, with the average value being determined. The microstructure of the two alloys was investigated using optical microscopy, EDS, EBSD, and TEM. To produce EDS samples, the Cu-0.3Zr-0.05Cr and Cu-0.3Zr-0.15Cr alloys underwent mechanical polishing. To create EBSD samples, the mechanically polished samples were subsequently electrochemically polished for one minute at room temperature in a 50% H_3PO_4 and 50% CH_3CH_2OH solution. For EBSD research, a JSM-7800 F field emission scanning electron microscope operating at 20 kV and with a step size of 5 μm was utilized. For TEM examinations, the alloy specimens were further thinned with a Gatan 691 ion milling machine after being polished to a thickness of 50 μm. The microstructure and distribution of precipitated phases within the alloy were examined using a JEM-2100 electron microscopy device running at 200 kV for TEM characterization.

Table 1
Composition of alloys.

Alloy	Alloy elements (wt%)		
	Zr	Cr	Cu
Cu-0.30Zr-0.05Cr	0.28	0.05	Bal.
Cu-0.30Zr-0.15Cr	0.27	0.16	Bal.

3. Results

3.1. Microstructure and properties

In order to optimize the properties of the alloys before the solid solution, the as-cast alloys were hot forged, and the microstructure of the Cu-0.3Zr-0.05Cr and Cu-0.3Zr-0.15Cr alloys in as-cast and hot forged states and after the solid solution is shown in Fig. 2. In cast Cu-0.3Zr-0.05Cr and Cu-0.3Zr-0.15Cr alloys, there are more intermetallic particles and larger internal grains.

It can be found comparing Fig. 2(a) and (b) with Fig. 2(d) and (e), that after the hot forging, the alloys undergo recrystallization, which produces equiaxed grains, and the internal grains undergo grain refinement, which optimizes the properties of the alloys. It can be found comparing Fig. 2(a) and (d), that the grain size of Cu-0.3Zr-0.05Cr alloy after hot forging is finer than the Cu-0.3Zr-0.15Cr alloy. The grains in Fig. 2(c) and (f) became larger after being treated with a solution at 900 °C. Some of the grains may include twins, which are indicated by arrows and could be annealing twins. The Cu-0.3Zr-0.05Cr alloy still has finer grain size than the Cu-0.3Zr-0.15Cr alloy.

In order to investigate the elemental composition of the dendrites present in the as-cast alloys, EDS experiments were carried out using the as-cast specimens. Fig. 3 shows the microscopic morphology of the as-cast microstructure of the two alloys. In Fig. 3(a) and (c), dendrite microstructure is found. The results of energy spectrum show that there is a high Zr element in the dendrites (Fig. 3(b) and (d)), indicating that Zr element exists aggregation phenomenon in the alloy and is not effectively dissolved in the matrix. This is consistent with the result that the as-cast structure has a high conductivity in Fig. 3(b), so in order to have a good effect of solid solution precipitation strengthening, solid solution treatment must be carried out.

Fig. 4 shows the properties of Cu-0.3Zr-0.05Cr and Cu-0.3Zr-0.15Cr alloys at various stages before aging. The hardness increases in Fig. 4(a) after hot forging due to the grain refinement. The alloy was further strengthened with dramatically increased hardness after hot forging treatment. However, grain growth occurs at high temperatures, decreasing the substrate hardness. The alloys are work-hardened by cold rolling. The Cu-0.3Zr-0.05Cr alloy hardness is 63 HV after solid solution, which increases to 142 HV after cold rolling. The Cu-0.3Zr-0.15Cr alloy hardness of 68 HV after the solid solution increases to 145 HV after cold working. Because of its finer internal grain size, the Cu-0.3Zr-0.05Cr alloy has a higher hardness in the hot forged state than the Cu-0.3Zr-0.15Cr alloy. The number of atoms from solid solution in the copper matrix has a strong correlation with the alloy's electrical conductivity [20]. As can be seen in Fig. 4(b), the electrical conductivity significantly decreased after the solution treatment. This shows that the matrix changes and scatters more free electrons as a result of the alloy's solid solution atoms dissolving in it, lowering the electrical conductivity. However, the conductivity of the alloy does not decrease significantly after cold rolling, because the dislocation has little effect on the conductivity of the alloy, so when the dislocation density in the alloy increases significantly, the conductivity of the alloy remains basically unchanged.

The Cu-0.3Zr-0.05Cr and Cu-0.3Zr-0.15Cr alloys' mechanical properties and electrical conductivity in different states are shown in Fig. 5 (a) and (c). The aging process is separated into three stages: under-aging, peak-aging, and over-aging. For instance, the hardness of the Cu-0.3Zr-0.05Cr alloy increases dramatically when it is aged at 450 °C. Several phases precipitate as a result of the alloy's internal supersaturated solid solution breakdown, which is occurring at this moment. This results in

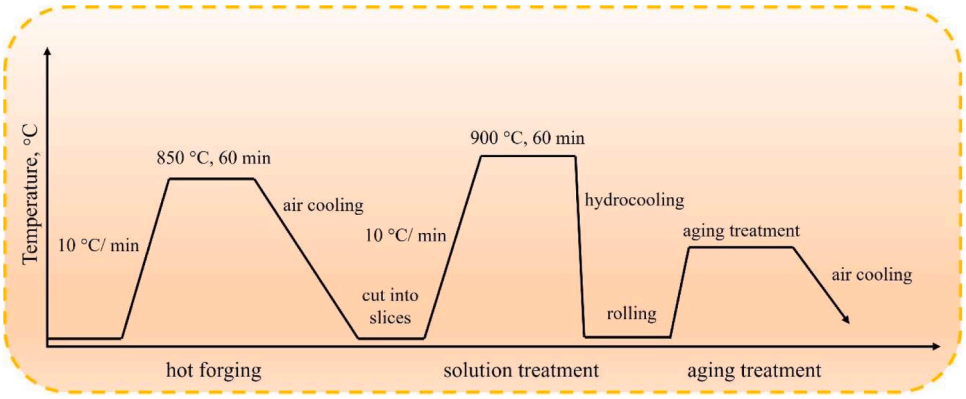

Fig. 1. Process flow diagram after alloy melting.

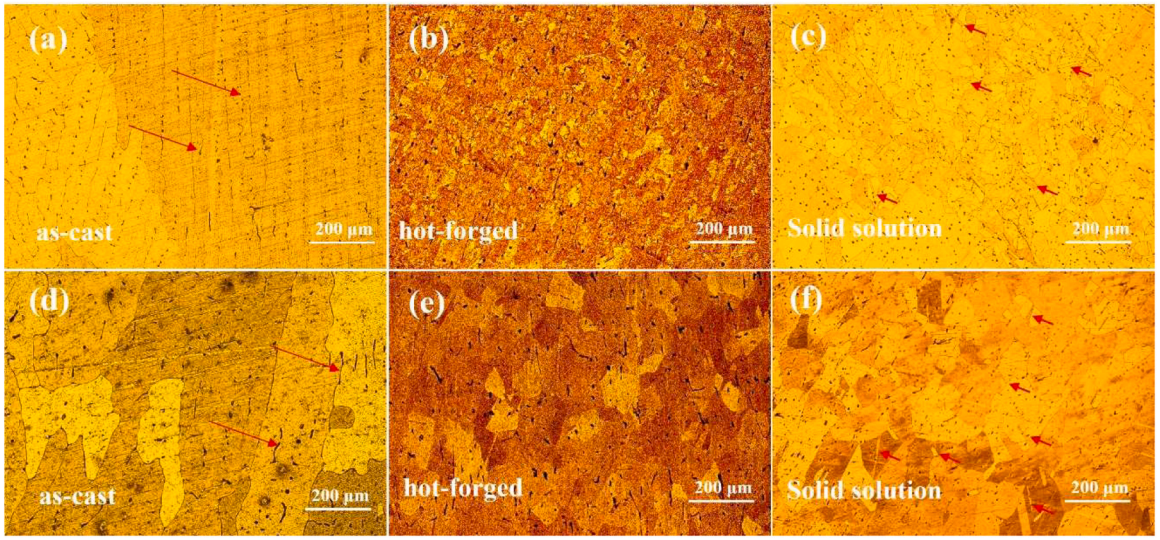

Fig. 2. Microstructure of the Cu-0.3Zr-0.05Cr and Cu-0.3Zr-0.15Cr alloys in different states: (a) as-cast Cu-0.3Zr-0.05Cr, (b) hot-forged Cu-0.3Zr-0.05Cr, (c) solid-solution Cu-0.3Zr-0.05Cr, (d) as-cast Cu-0.3Zr- 0.15Cr, (e) hot-forged Cu-0.3Zr-0.15Cr, (f) solid-solution Cu-0.3Zr-0.15Cr.

precipitation reinforcement. On the other hand, the alloy experiences less of a softening effect during the aging treatment when it is aged for a shorter amount of time. Thus, the hardness of the alloy rises rapidly, and this stage is the under-aged stage. The alloy reaches a peak hardness of 163 HV in 60 min, which is the result of the synergistic effects of precipitation and work-hardening, which is the peak aging stage. With further aging, the work-hardening effect produced by cold deformation is gradually weakened by high temperature, which leads to a rapid decrease in the hardness. At the same time, at the late aging stage, the precipitated phases grow in size with aging, leading to a continuous hardness decrease. As can be shown in Fig. 5(b) and (d), during the early stage of aging, the electrical conductivity of the alloy increases dramatically due to the breakdown of the supersaturated solid solution in the matrix and the precipitation of a high number of solid solution atoms.

Simultaneously, it was discovered that, during the same aging duration, the alloy's conductivity increased with increasing aging temperature. This is because higher aging temperatures accelerate precipitation. However, when the temperature is too high, the "Osterwald curing [21,22]" phenomenon may occur in the alloy, resulting in the precipitation phase produced by the alloy redissolving into the matrix, resulting in low conductivity. This is the reason why the conductivity of 550 °C in Fig. 5(b) is lower than that of 450 °C and 500 °C. Both Cu-0.3Zr-0.05Cr and Cu-0.3Zr-0.15Cr alloys have the highest alloy hardness when aged at 450 °C. After 60 minutes at 450 °C aging, the Cu-0.3Zr-0.05Cr alloy reaches a peak hardness of 163 HV and an electrical conductivity of 74.4% IACS. The Cu-0.3Zr-0.15Cr alloy showed outstanding overall mechanical properties, with a peak hardness of 180 HV and an electrical conductivity of 84.4% IACS after being aged at 450 °C for 120 minutes. Fig. 5(e) shows the peak hardness of Cu-0.3Zr-0.15Cr alloy at various temperatures and aging time. Peak hardness rose first and subsequently fell as the aging temperature rose. Low hardness is the result of the aging temperature being too low to fully precipitate the precipitated phase. An excessive increase in temperature will lead to severe softening or even recrystallization of the alloy, which will lower its hardness. Additionally, it is discovered that at all temperatures, the alloy requires less time to reach its peak hardness. This is due to the fact that a greater temperature causes precipitation to occur more often, which shortens the amount of time needed for the alloy to reach its peak hardness. Fig. 5(f) shows the tensile strength of the two alloys aged at 450 °C.

The Cu-0.3Zr-0.05Cr alloy was aged at 450 °C for a total of 30 minutes, an hour, and two hours. The corresponding elongation is 13.3%, 10% and 11.7%, the tensile strength is 440 MPa, 442 MPa and 420 MPa, and the corresponding yield strength is 394 MPa, 382 MPa and 395 MPa, respectively. The Cu-0.3Zr-0.15Cr alloy was aged at the temperature of 450 °C for 60, 120, and 240 minutes. The tensile strength is 439 MPa, 467 MPa and 458 MPa, the yield strength is 390 MPa, 413 MPa and 394 MPa, and the elongation is 13.1%, 12.1% and 11.6%, respectively. The trend of strength changes for both alloys is first

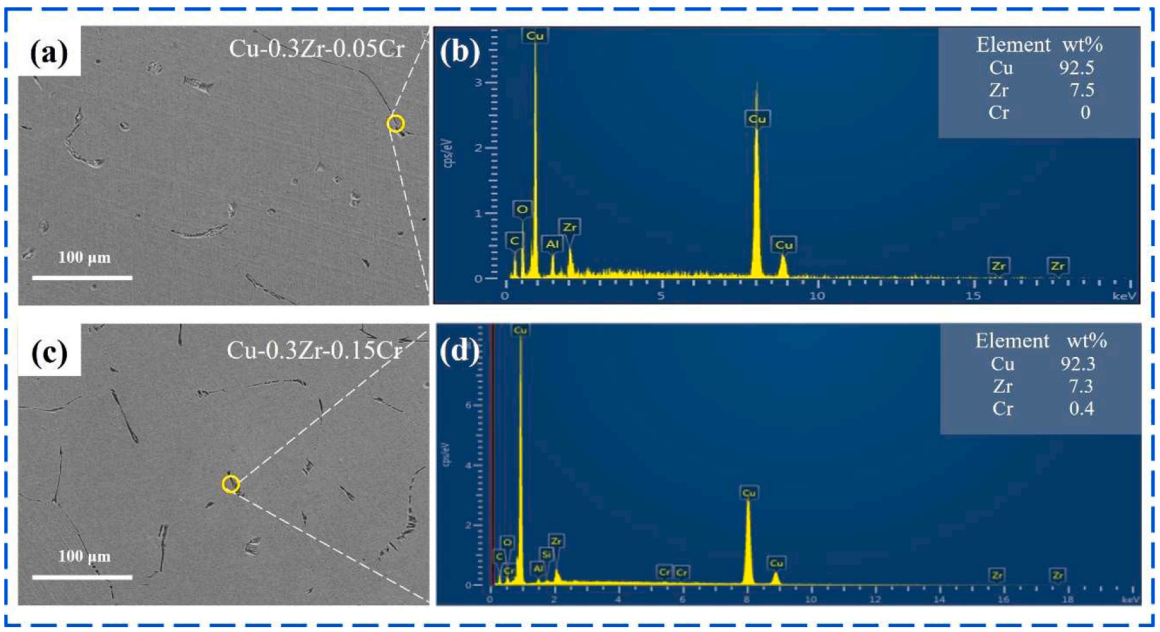

Fig. 3. Microstructure of the two alloys in as-cast state: (a) SEM image of Cu-0.3Zr-0.05Cr alloy; (b) Spectral analysis of Cu-0.3Zr-0.05Cr alloy dendritic region; (c) SEM image of Cu-0.3Zr-0.15Cr alloy; (d) Line scanning spectral analysis of Cu-0.3Zr-0.15Cr alloy dendritic region.

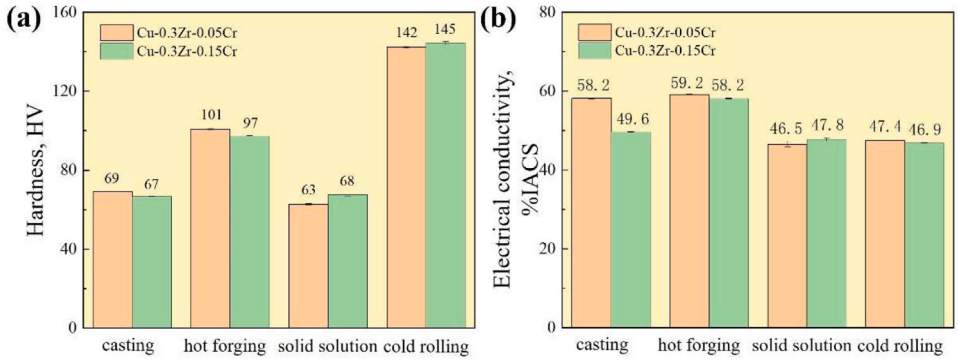

Fig. 4. The properties of Cu-0.3Zr-0.05Cr and Cu-0.3Zr-0.15Cr alloys at different stages: (a) Hardness after four processes, (b) Electrical conductivity after four processes.

increasing and then decreasing, which is the same as the trend of microhardness change and opposite to the elongation trend.

Finally, the optimal aging parameters for both alloys were discovered. For the Cu-0.3Zr-0.05Cr alloy, the ideal aging parameters are: 450 °C aging temperature, 60 min aging time, 163 HV microhardness, 442 MPa tensile strength, 74.4% IACS electrical conductivity, and 10% elongation. For the Cu-0.3Zr-0.15Cr alloy, the ideal aging parameters are: 450 °C aging temperature, 120 min aging time, 180 HV microhardness, 467 MPa tensile strength, 84.4% IACS electrical conductivity, and 12.1% elongation.

3.2. EBSD analysis

The samples at the peak hardness of the two alloys and the samples at the over-aging stage were chosen for EBSD tests in order to investigate the change in the microstructure of the alloy with the extension of the aging duration. Fig. 6 presents the findings. The graphic indicates that there are two primary orientations for the alloy's grain orientation in each of the four states: <001> and <101> direction. Fig. 6(a) is the EBSD diagram and grain size diagram of Cu-0.3Zr-0.05Cr alloy aged at 450 °C for 60 min. According to the statistics of the data, the average grain size of the alloy is 42 μm, and 7.1% of the grain size is greater than 100μm. Fig. 6(b) displays the EBSD graph and the size of the grain diagram of the Cu-0.3Zr-0.05Cr alloy after it has been aged for 360 minutes at 450°C.The average grain size of Cu-0.3Zr-0.05Cr alloy at this time is 68 μm. While the average particle size grows from 42 μm to 68 μm, the percentage of grains with a size larger than 100 μm increases from 7.1% to 28.3%. The main reason is that the aging time of the latter is longer and the grains grow.

The Cu-0.3Zr-0.15Cr alloy's EBSD and grain size diagrams are displayed in Fig. 6(c) and (d), following 120 and 360 minutes of age at 450 °C. The picture illustrates how the alloy's average grain size increases from 174 μm to 241 μm as aging time is extended, and how the percentage of grain size greater than 100 μm increases from 57.9% to 66.6%. The finer the grain is, the better the fine grain strengthening effect of the alloy is, which is one of the reasons why the hardness of Cu-0.3Zr-0.15Cr alloy aged at 450 °C for 120 min is higher than that aged at 360 min.

The literature states that GOS values above 15° are linked to deformed or recrystallized grains, whereas values below 15° are linked to subgranularity of the tissue [23,24]. The GOS diagrams of Cu-0.3Zr-0.05Cr and Cu-0.3Zr-0.15Cr alloys under different aging parameters are generated in Fig. 7. After cold deformation aging, when the temperature rises, the alloy will recrystallize, and the longer the aging

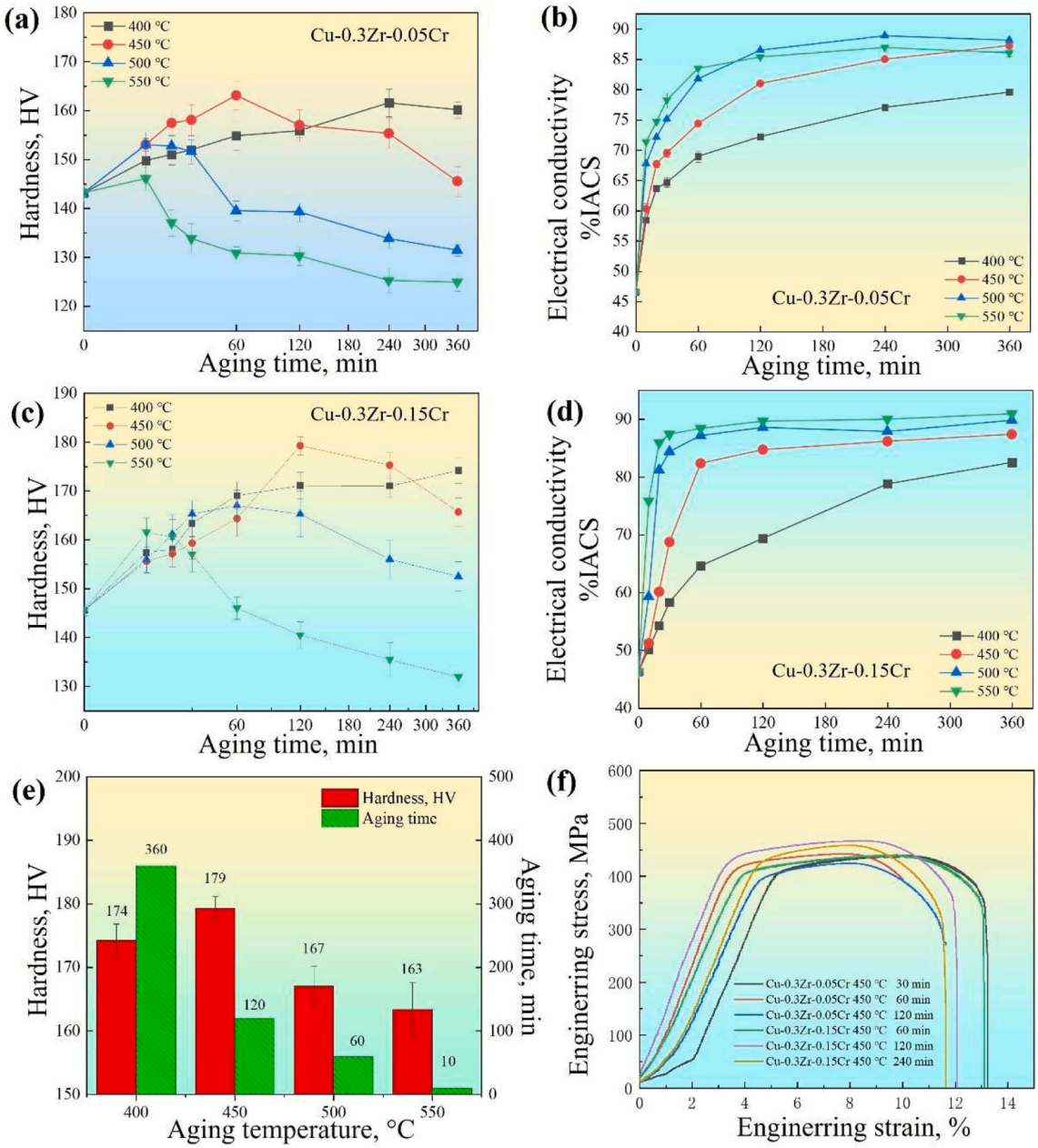

Fig. 5. Mechanical characteristics and electrical conductivity of Cu-0.3Zr-0.05Cr and Cu-0.3Zr-0.15Cr alloy after different aging processes: (a) Hardness of Cu-0.3Zr-0.05Cr alloy, (b) Electrical conductivity of Cu-0.3Zr-0.05Cr alloy, (c) Hardness of Cu-0.3Zr-0.15Cr alloy, (d) Electrical conductivity of Cu-0.3Zr-0.15Cr alloy, (e) Peak hardness and time at different aging temperatures of Cu-0.3Zr-0.15Cr alloy, (f) Stress-strain curves for engineering in both alloys.

time, the more the recrystallization region, so the content of the red region increases. Fine recrystallization can optimize the properties of the alloy, but coarsening occurs with the extension of aging time, which has an adverse effect on the properties of the alloy. This is related to the decrease of strength and plasticity of the alloy in the over-aging stage.

After 60% cold rolling, the alloy's dislocation density significantly rises due to the work hardening effect, strengthening the alloy. However, after the aging treatment, the alloy will soften to a certain extent, and the dislocation density inside the alloy will decrease. In order to study the effect of aging time on the dislocation density of the alloy, the EBSD data in Fig. 6 were processed and the KAM diagram was obtained. Fig. 8 is the KAM diagram of Cu-0.3Zr-0.05 Cr and Cu-0.3Zr-0.15 Cr alloys under different aging processes. The alloy's dislocation density can be computed using the KAM diagram :

$$\rho = 2\theta/\mu b \quad (1)$$

In this case, ρ represents the alloy's density of dislocations (m^{-2}), θ stands for the alloy's average orientation angles (rad), μ is the scanner step length (μm), and b is the copper's Burger vector (0.255 nm).

Following computation, the Cu-0.3Zr-0.05 Cr alloy with ages at 450 °C for 60 and 360 minutes had dislocation densities of $\rho = 6.49 \times 10^{13}$ m^{-2} and $\rho = 6.40 \times 10^{13}$ m^{-2}, accordingly. Likewise, after aging at 450 °C for 120 and 360 minutes, the dislocation densities of the Cu-0.3Zr-0.15Cr alloy are $\rho = 6.5 \times 10^{13}$ m^{-2} and $\rho = 6.63 \times 10^{13}$ m^{-2}, respective. It can be found that the dislocation density of the alloy increases when the Cr content is higher.

To examine the textural evolution of Cu-0.3Zr-0.05Cr and Cu-0.3Zr-0.15Cr alloys during a wider aging period, Fig. 9 displays the polar coordinates of the two alloys. By contrasting the typical pole Fig. [25], it can be seen that the Cu-0.3Zr-0.05Cr alloy mainly contains Brass texture and S texture at 60 min, and the main texture after aging for 360 min is Brass texture. It can be seen from Fig. 9(c) and Fig. 9(d) that the main

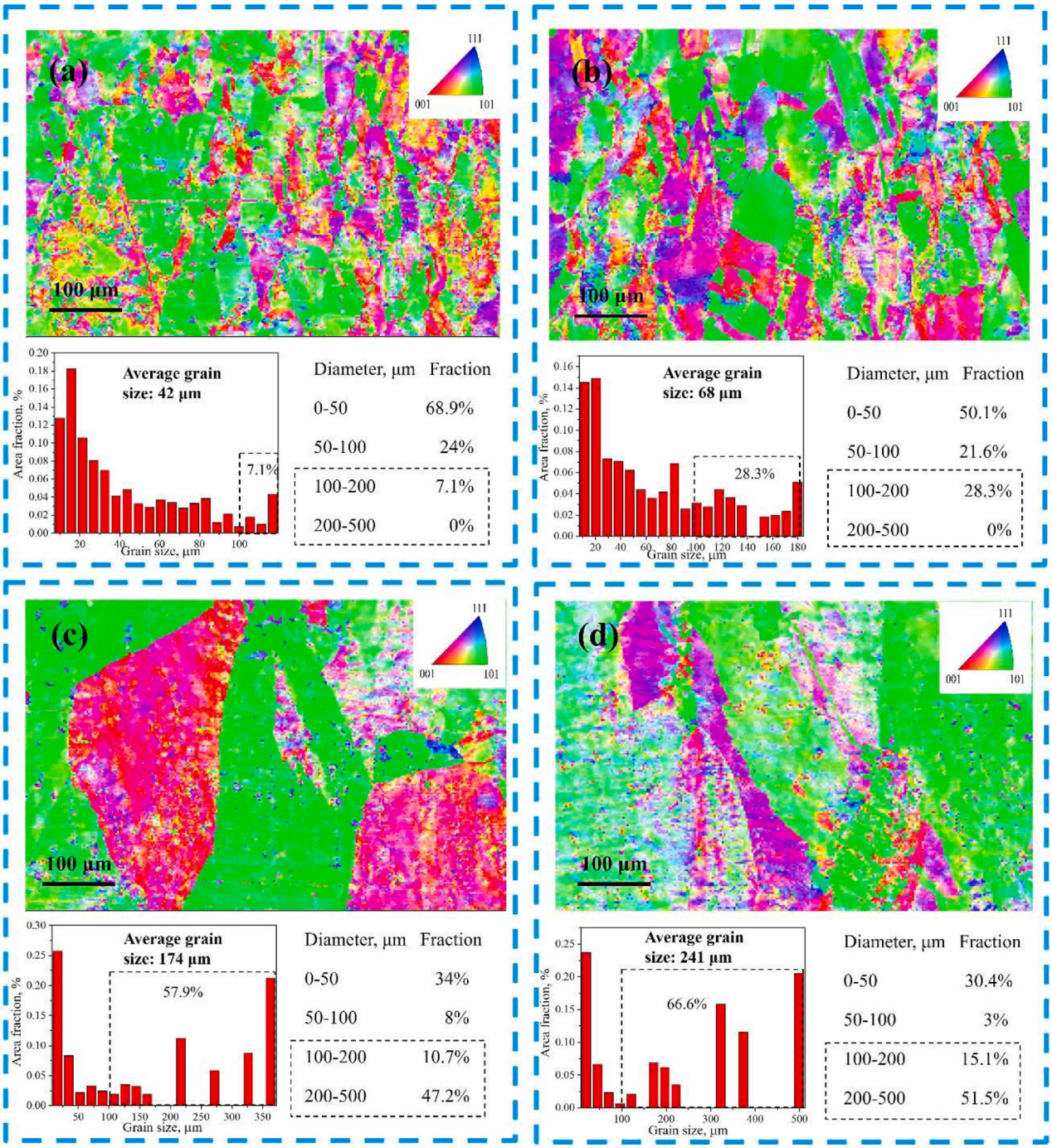

Fig. 6. Cu-0.3Zr-0.05Cr and Cu-0.3Zr-0.15Cr alloys aged at 450 °C: EBSD and grain size diagrams: (a) Cu-0.3Zr-0.05Cr alloy aged for 60 min, (b) Cu-0.3Zr-0.05Cr alloy aged for 360 min, (c) Cu-0.3Zr-0.15Cr, (c) Cu-0.3Zr-0.15Cr alloy aged 120 min, (d) Cu-0.3Zr-0.15Cr alloy aged 360 min.

texture of Cu-0.3Zr-0.15Cr alloy at 120 min is Goss texture and S texture, while the main texture of the alloy after aging for 360 min is transformed into Brass texture and S texture. It is discovered that when the alloy ages longer, its main texture changes.

Fig. 10 is the texture composition diagram and content comparison diagram of Cu-0.3Zr-0.05Cr and Cu-0.3Zr-0.15Cr alloys aged at 450 °C. Fig. 10 (a) shows the texture map of Cu-0.3Zr-0.05Cr alloy aged at 450 °C for 60 min. The texture content from more to less is Brass, S, copper, Goss and Cube texture, and the corresponding texture content is 21.9%, 20.8%, 11.6%, 10.2% and 4.05%, respectively. Fig. 10 (b) shows the texture composition diagram of Cu-0.3Zr-0.15Cr alloy after aging at 450 °C for 120 min. The texture content from more to less is Goss, S, copper, Brass and Cube, and the corresponding proportions are 30.1%, 21.4%, 20.1%, 16.7% and 4.74%, respectively. It can be found that the textures with texture content greater than 20% of the former are S and Brass texture, and the textures with texture content greater than 20% of the latter are Goss, copper and S texture, which essentially agree with the findings of Fig. 9(a) and (c). Fig. 10 (c) is the texture content comparison diagram of Cu-0.3Zr-0.05Cr alloy aged at 450 °C for 60 min and 360 min. It can be found that the content of various textures decreases with the increase of aging time, which is caused by the recovery of the alloy during aging. Fig. 10 (d) is the texture content comparison diagram of Cu-0.3Zr-0.05Cr and Cu-0.3Zr-0.15Cr alloys aged at 450 °C for 360 min. It can be seen that when the content of Cr is different, the

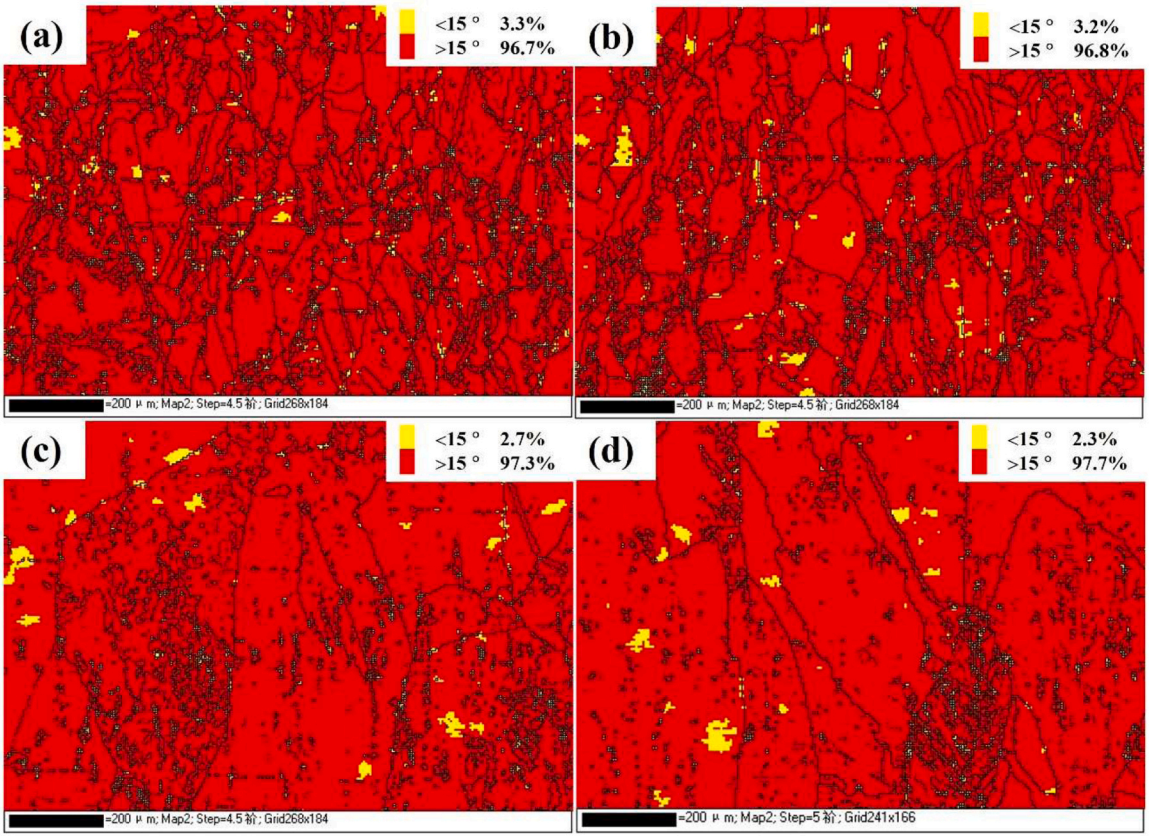

Fig. 7. Grain orientation spread plots of the Cu-0.3Zr-0.05Cr and Cu-0.3Zr-0.15Cr alloys after different aging processes: (a) Cu-0.3Zr-0.05Cr alloy aged for 60 min, (b) Cu-0.3Zr-0.05Cr alloy aged for 360 min, (c) Cu-0.3Zr-0.15Cr alloy aged for 120 min, (d) Cu-0.3Zr-0.15Cr alloy aged for 360 min.

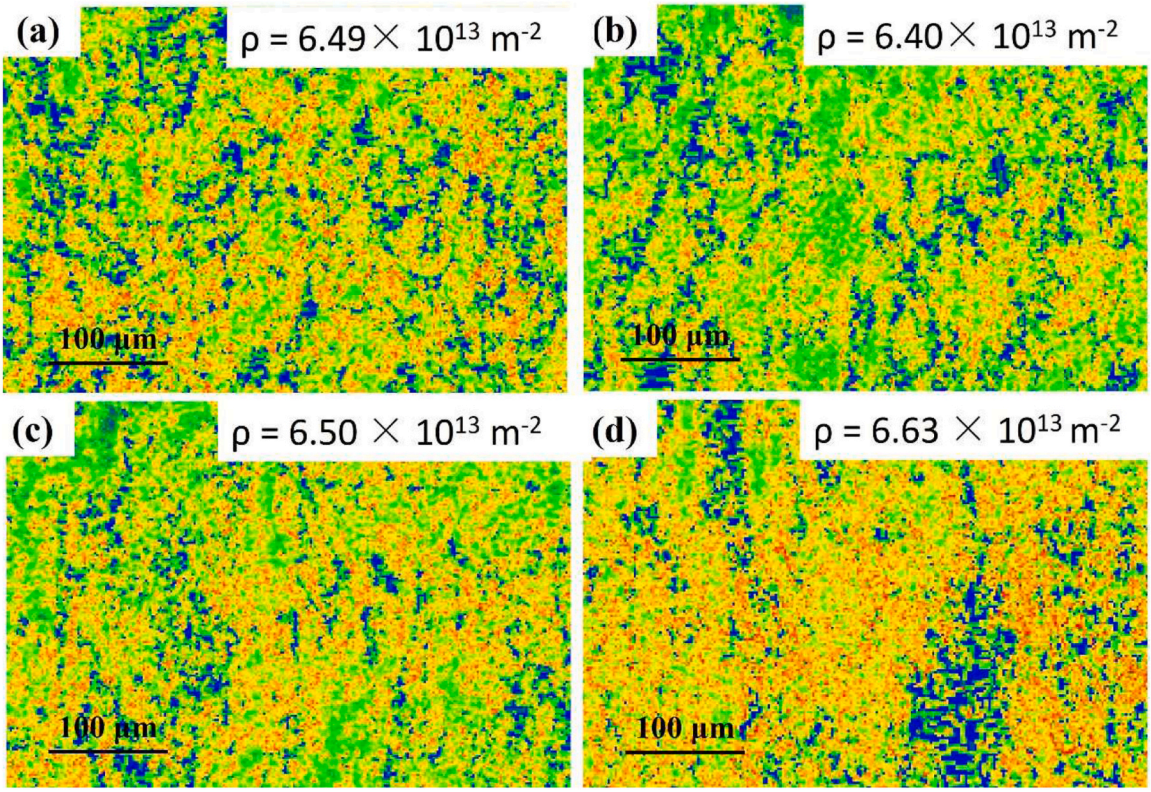

Fig. 8. Kernel average misorientation angle maps of Cu-0.3Zr-0.05Cr and Cu-0.3Zr-0.15Cr alloys under different aging processes: (a) Cu-0.3Zr-0.05Cr alloy aged for 60 min, (b) Cu-0.3Zr-0.05Cr alloy aged for 360 min, (c) Cu-0.3Zr-0.15Cr alloy aged 120 min, (d) Cu-0.3Zr-0.15Cr alloy aged 360 min.

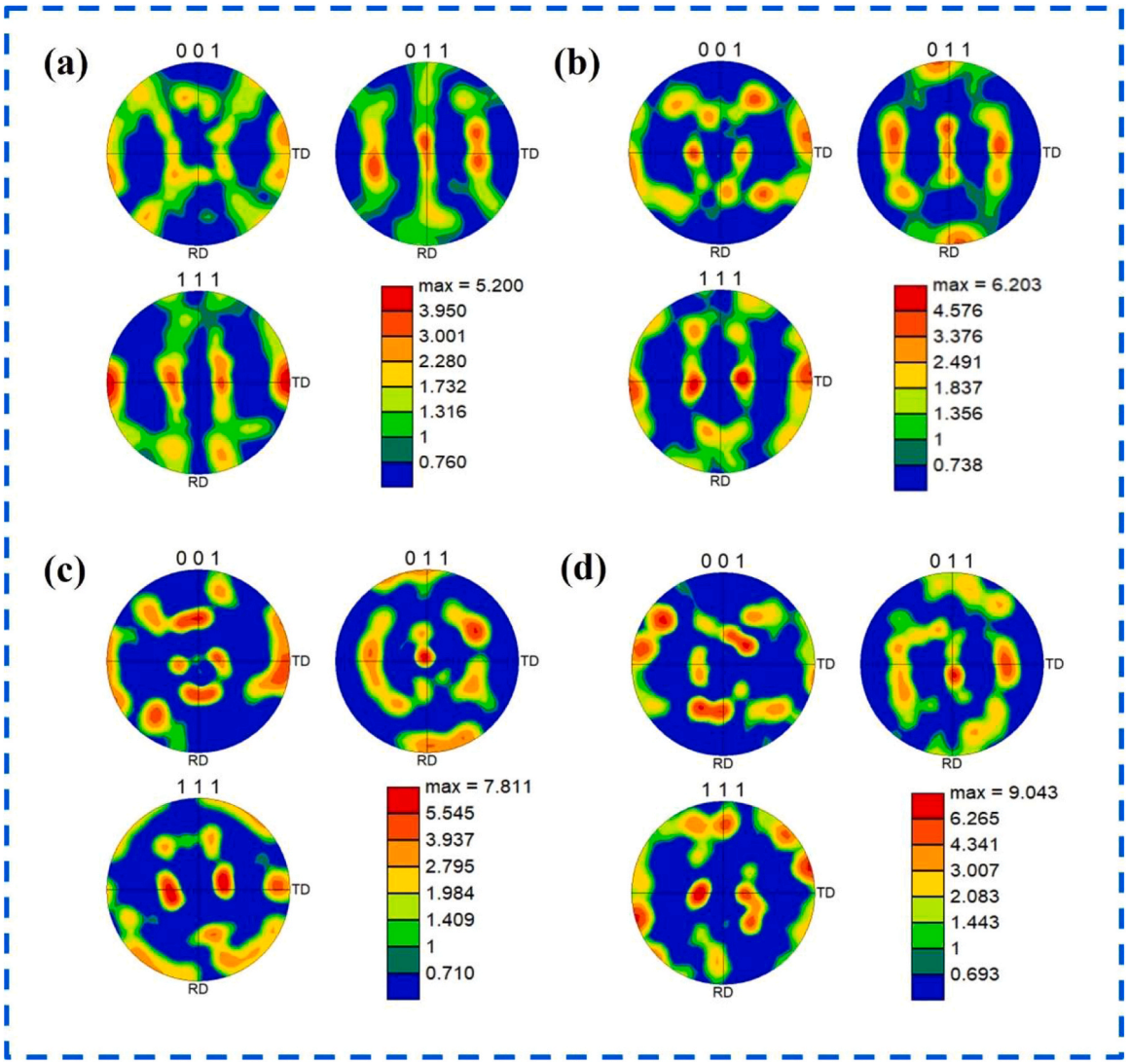

Fig. 9. Pole figures of the Cu-0.3Zr-0.05Cr and Cu-0.3Zr-0.15Cr alloys aged at different conditions: (a) Cu-0.3Zr-0.05Cr alloy aged for 60 min, (b) Cu-0.3Zr-0.05Cr alloy aged for 360 min. (c) Cu-0.3Zr-0.15Cr alloy aged 120 min, (d) Cu-0.3Zr-0.15Cr alloy aged 360 min.

texture content will be very different. The corresponding proportions of Goss, Cube, copper, Brass and S textures of Cu-0.3Zr-0.05Cr alloy aged for 360 min are 1.04%, 2.96%, 0.88%, 9.22% and 2.01%, respectively. When the Cu-0.3Zr-0.15Cr alloy is aged for 360 min, the corresponding proportions of Goss, Cube, copper, Brass and S textures are 21.6%, 0.7%, 3.74%, 33.5% and 31.5%, respectively. It is found that the addition of more Cr will make the alloy contain more Goss, Brass, copper and S textures in the over aging stage after cold rolling, which may be related to the fact that the Cu-0.3Zr-0.15Cr alloy can retain more textures after aging for 360 min. This could also be a contributing factor to Cu-0.3Zr-0.15Cr alloy's superior performance over Cu-0.3Zr-0.05Cr alloy.

3.3. TEM analysis

The Cu-0.3Zr-0.05Cr alloy's TEM diagram, aged for 60 minutes at 450 °C, is shown in Fig. 11. From Fig. 11 (a), (b) and (c), it can be seen that there are fine and uniform distribution of nano-precipitates in Cu-0.3Zr-0.05Cr alloy. At the same time, there are dislocation walls, dislocation tangles, dislocation cells and other microstructures. The strength of the alloy greatly benefits from these structures [26,27]. The electron diffraction pattern of Fig. 11(c) in the specified area is shown in Fig. 11(d). Through calibration, it can be determined that there are two precipitated phases, Cr phase and Cu_5Zr phase, in the copper matrix. This shows that after aging treatment, the alloy elements in the alloy are precipitated in the form of Cr phase and Cu_5Zr phase, respectively. The precipitated phase's precipitation significantly reduces the alloy's internal lattice distortion, which lessens the alloy's resistance to free electrons and significantly increases the alloy's electrical conductivity [28].

HRTEM images and fast Fourier transform (FFT) maps of the Cu-0.3Zr-0.05Cr alloy are displayed in Fig. 11(e) and (f), where a Cu matrix with nanoscale precipitates of the Cr phase was found by calibration to obtain three crystalline surfaces $(1\bar{1}1)$ Cr, $(1\bar{1}1)$ Cr, and (002) Cr with three crystalline surfaces $(1\bar{1}1)$ Cu, $(11\bar{1})$ Cu, and (020) Cu. The inverse FFT (IFT) diagrams of nanoscale Cr are displayed in Fig. 11(g_1-g_3). The spacing of the $(1\bar{1}1)$ Cr crystalline planes is 0.261 nm, 0.2618 nm for the $(1\bar{1}1)$ Cr crystalline planes, and 0.2353 nm for the (002) Cr crystalline planes. Similarly, the crystal plane spacing of $(1\bar{1}1)$Cu can be obtained as 0.24 nm in Fig. 11(h1), $(11\bar{1})$ Cu has a crystal plane spacing of 0.2196 nm in Fig. 11(h_2), and (020) Cu has a crystalline plane spacing of 0.198 nm in Fig. 11(h_3). Some dislocations (yellow "T"-shaped regions) are found in the inverse FFT diagram, which distort the lattice and affect the strength and conductivity. Cu $(1\bar{1}1)$ lattice spacing is 0.2249 nm and Cr $(1\bar{1}1)$ lattice spacing is 0.261 nm. The misfit of the interface between the Cu matrix and the Cr nano-precipitated phase is $\delta = \frac{2(d_\alpha - d_\beta)}{(d_\alpha + d_\beta)} =$

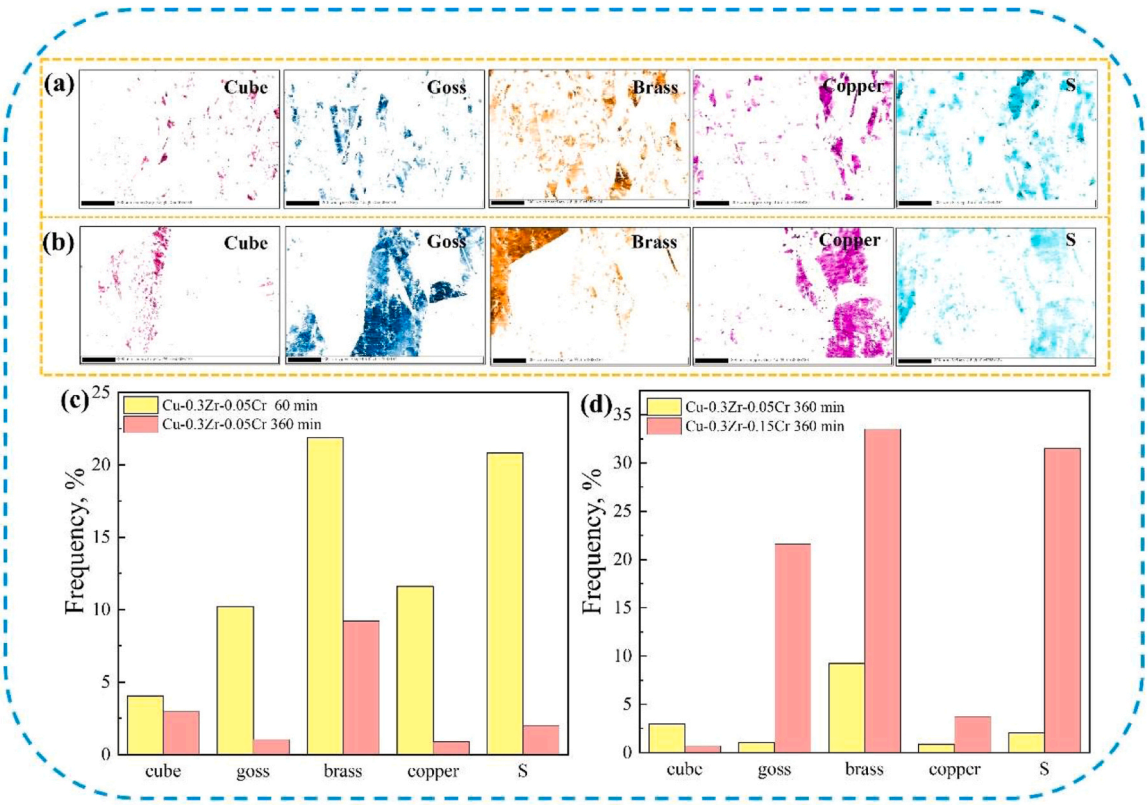

Fig. 10. Texture composition of the Cu-0.3Zr-0.05Cr and Cu-0.3Zr-0.15Cr alloys aged at 450 °C: (a) Cu-0.3Zr-0.05Cr alloy aged for 60 min, (b) Cu-0.3Zr-0.15Cr alloy aged for 120 min. (c) Texture comparison of the Cu-0.3Zr-0.05Cr alloy aged for 60 min and 360 min, (d) Comparison of the two alloys' textures after 360 minutes of aging.

$\frac{2\times(0.2610-0.2400)}{(0.2610+0.2400)}\times$ 100%=8.38%<15%. The interface is semi-coherent, where d_α and d_β are the crystal plane spacing of $(1\bar{1}\bar{1})$ Cr and $(1\bar{1}\bar{1})$ Cu parallel planes, respectively. Reduced elastic stress and interface energy are produced by a semi-coherent connection with low mismatch, which is crucial for enhancing the alloy's strength and plasticity [29]. Fig. 11(i) shows the statistical diagram of particle size of the precipitated phase in the Cu-0.3Zr-0.05Cr alloy. The proportion of the 2–3 nm precipitated phase is the largest, and the average precipitated phase size is d_p=2.8 nm.

The TEM picture of the Cu-0.3Zr-0.15Cr alloy, aged for 120 minutes at 450°C, is displayed in Fig. 12. The bright field images presented in Fig. 12(a-c) demonstrate the presence of sub-grain boundaries, dislocation cells, and dislocation walls in addition to a multitude of finely distributed and uniformly sized nano-precipitated phases in the Cu-0.3Zr-0.15Cr alloy. After calibration, selected-area electron diffraction in Fig. 12(c) revealed the presence of two precipitated phases in the copper matrix: Cr and Cu_5Zr. The $(\bar{1}3\bar{1})$ crystal plane spacing is d=0.1151 nm for copper, d=0.1277 nm for Cr $(11\bar{3})$, and d=0.2563 nm for Cu_5Zr $(0\bar{2}2)$. The mismatch between nano-precipitated Copper substrate and Chromium phase is $\delta = \frac{2(d_\alpha-d_\beta)}{(d_\alpha+d_\beta)} = \frac{2\times(0.1277-0.1151)}{(0.1277+0.1151)}\times$ 100%=10.38%, which is greater than the mismatch between the Copper substrate and Chromium phase of the Cu-0.3Zr-0.05Cr alloy. Fig. 12(e) shows the particle size statistics of the precipitated phase in the Cu-0.3Zr-0.15Cr alloy. The majority of the precipitated phases were made up of particles that were between 2 and 5 nm in size, with an average size of d_p = 3.4 nm.

The average size of precipitated phases increased by a factor of 1.2 compared with Fig. 12(i). The reason for the greater misfit δ between the Chromium phase and the Copper matrix of the nano-precipitated phase in the Cu-0.3Zr-0.15Cr alloy is likely due to the latter's somewhat longer aging time, which gave the precipitated phases plenty of opportunity to grow. In addition to increasing the alloy's strength and hardness, the precipitated phase also lessens matrix lattice distortion, lessens barriers to free electrons, and enhances the alloy's electrical conductivity. [30].

4. Discussion

4.1. Cr contents effects on texture and precipitation behavior

When other factors remain unchanged, the finer the grain, the greater the resulting grain boundary strengthening, and the better the alloy performance, as seen in Fig. 3. Higher Cr content in the alloy results in coarser recrystallized grains, associated with grain boundary weakening. The sort, strength, and amount of texture in the alloy have an immediate association with its properties [31]. The content of Brass texture in the Cu-0.3Zr alloy during peak aging decreases significantly with Cr content, the Goss and copper texture increases significantly, and the maximum texture strength of the alloy also increased from 5.2 to 7.8 in Fig. 7. During over-aging, the Brass, S, and Goss texture increased dramatically as the Cr content increased from 0.05 wt% to 0.15 wt%, while the other texture did not change much, and the maximum texture strength increased from 6.2 to 9. Consequently, after age, the alloy's maximum texture intensity value and Goss texture content will both greatly increase as the Cr content rises from 0.05 wt percent to 0.15 wt percent. This has a significant impact on the alloy's properties. On the other hand, the amount of Cr in the alloy also has a very important effect on the precipitation behavior. It can be seen from Fig. 11(c) and (c) that the Cu-0.3Zr-0.15Cr alloy contains more nanoscale precipitates, which indicates that the higher the Cr content, the more precipitates will form during aging. The resulting precipitation strengthening is stronger, so the Cu-0.3Zr-0.15Cr alloy has a higher strength.

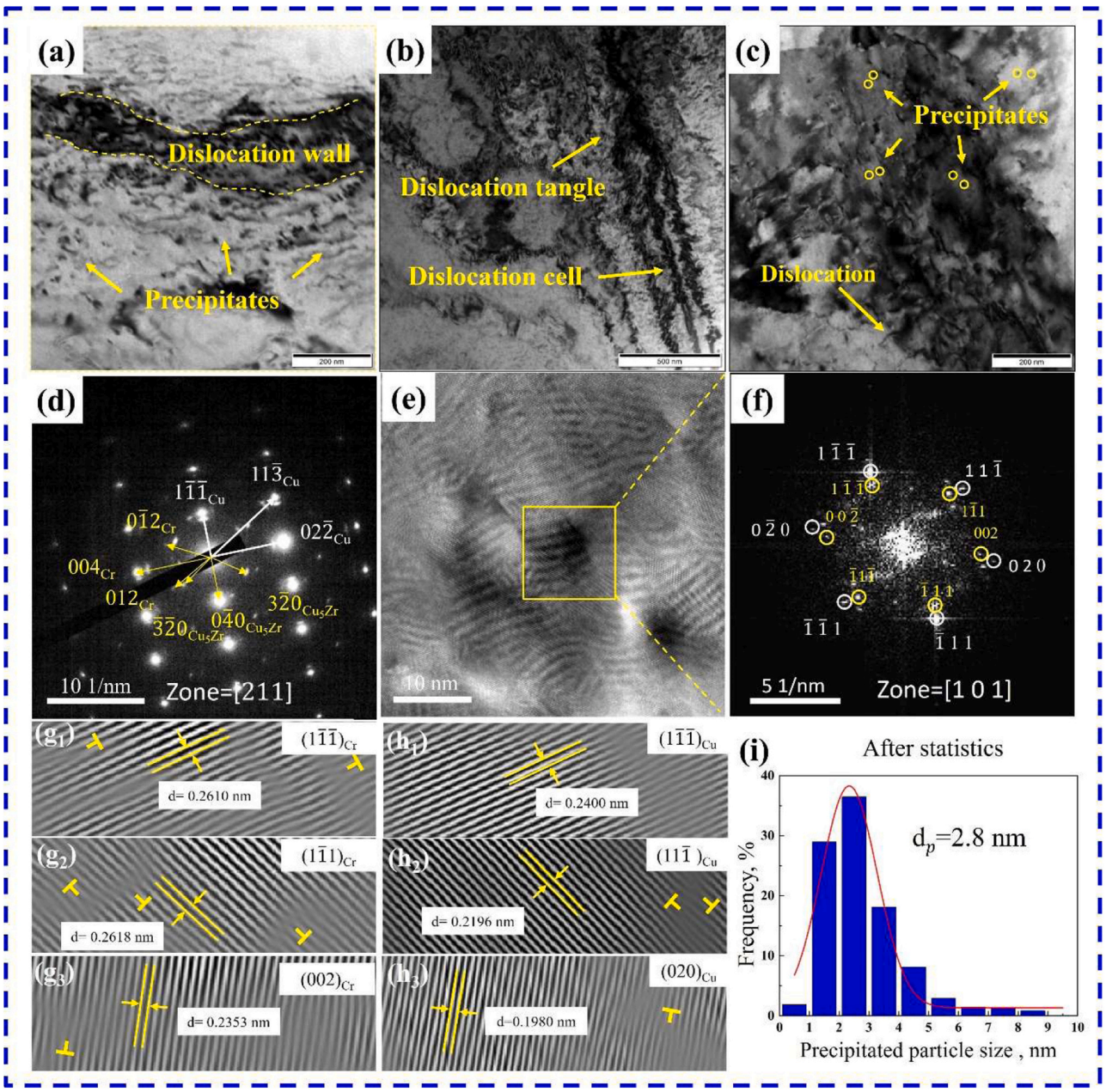

Fig. 11. TEM images of the Cu-0.3Zr-0.05Cr alloy aged at maximum hardness: (a-c) bright-field images; (d) selected electron diffraction; (e) HRTEM image; (f) FFT pattern of Cu and Cr; (g) IFT pattern of Cr: (g1) $(1\bar{1}\bar{1})$, (g2) $(1\bar{1}1)$, (g3) (002); (h) inverse FFT of the Cu matrix: (h1) $(1\bar{1}\bar{1})$, (h2) $(11\bar{1})$, (h3) (020); (i) particle size statistics of precipitated phase.

4.2. *Strengthening mechanisms*

The four aspects of solid solution strengthening, deformation strengthening, grain boundary strengthening, and precipitation strengthening are responsible for the high strength of copper alloys. However, since the Zr and Cr solid solution atoms in the matrix have precipitated out in large quantities after the alloy has aged for a long time, the value of the contribution to the strength of the solid solution strengthening is neglected. As a result, the Cu-0.3Zr-0.15Cr alloy's strength σ is composed of the following four components [31]:

$$\sigma = \sigma_0 + \sigma_{ds} + \sigma_p + \sigma_{GB} \tag{2}$$

Here, σ_0 represents the Cu matrix's lattice friction stress, which is 20 MPa.

The hardening stress is σ_{ds}, the precipitation strengthening stress is σ_p, and the grain boundary strengthening stress is σ_{GB}. The following is an expression of the effect of reinforcing grain boundaries using the Hall-Petch formula [32]:

$$\sigma_{GB} = K_y d^{-1/2} \tag{3}$$

In this instance, d is the average grain size (d=174 μm) for the Cu-0.3Zr-0.15Cr alloy. K_y is the Hall-Petch coefficient, which is 150 MPa $\mu m^{1/2}$. It is determined that the Cu-0.3Zr-0.15Cr alloy has a grain-boundary strengthening σ_{GB} of 11.4 MPa. The Cu-0.3Zr-0.05 Cr alloy exhibits a 23.2 MPa grain boundary strengthening. After undergoing solution treatment, the Cu-0.3Zr-0.15Cr alloy was cold rolled with 60% deformation to increase its hardness and strength. The copper matrix was reinforced by the dislocation cells, sub-grain boundaries, and other features formed during the cold rolling process. The following is a description of the impact of deformation strengthening [33]:

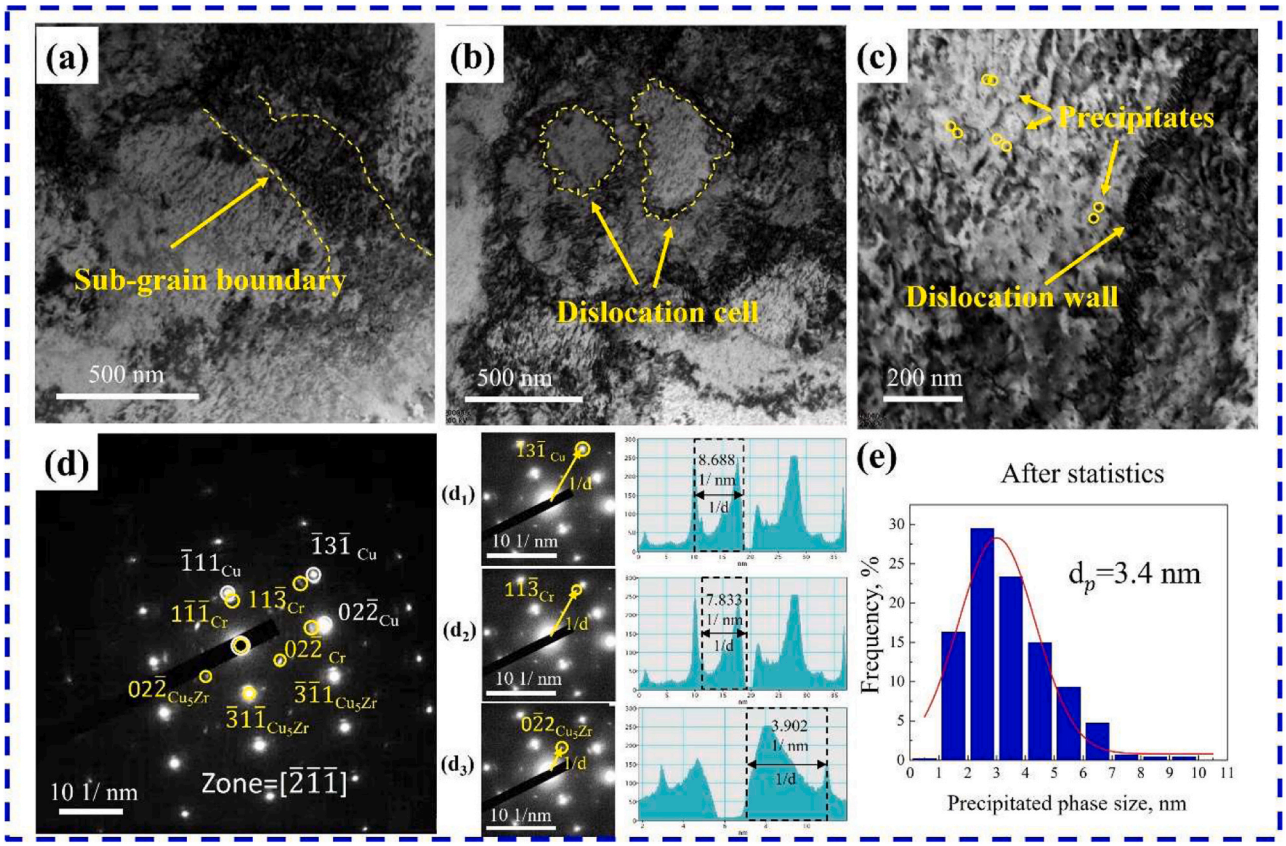

Fig. 12. TEM images of the Cu-0.3Zr-0.15Cr alloy aged at maximum hardness: (a-c) bright-field images; (d) Selected electron diffraction patterns: (d_1) $(\bar{1}3\bar{1})_{Cu}$, (d_2) $(11\bar{3})_{Cr}$, (d_3) $(0\bar{2}\bar{2})_{Cu5Zr}$; (e) particle size statistics of precipitated phase.

$$\sigma_{ds} = M\alpha Gb\sqrt{\rho} \tag{4}$$

Here, b represents the Burgers vector (0.2556 nm), ρ is the alloy's dislocation density, which is found using the KAM diagrams, G is the shear modulus, and α is the geometric constant (0.3). M is the Taylor coefficient (3.06) of the alloy. Accordingly, the Cu-0.3Zr-0.15Cr alloy's deformation strengthening is $\sigma_{ds} = 87.3$ MPa, while the Cu-0.3Zr-0.05Cr alloy's deformation strengthening is 87 MPa. In the Cu-0.3Zr-0.15Cr alloy, the kind and size of precipitated phases as well as the interaction between them and dislocations are crucial factors in the alloy's strengthening. Generally speaking, there are two ways in which the precipitated phase and dislocations interact: dislocation bypassing and particle shearing. Since the shear mechanism typically occurs when the precipitated phase is co-lattice with the matrix, and the dislocation bypassing mechanism primarily occurs when the precipitated phase is semi- or non-co-lattice with the matrix, the dislocation bypassing mechanism (the Orowan-Ashby equation) is thought to be the strengthening mechanism of this alloy [34]. Its impact on the precipitation strengthening can be explained as follows [35]:

$$\sigma_p = \frac{0.8MGb}{2\pi\sqrt{1-\upsilon}\lambda}\ln\left(\frac{x}{2b}\right) \tag{5}$$

$$x = \sqrt{\frac{2}{3}}d \tag{6}$$

where M is the Taylor factor (taken as 3.06), G is the shear modulus of the Cu matrix (46 GPa), b is the Burgers vector of Cu (0.2556 nm), υ is the Poisson's ratio (0.34), d is the average particle size within the Cr particles, and the results of the statistical results are shown in Fig. 8. λ is the average distance between precipitates, obtained from a large number of statistics "distance between the nearest two precipitates", and its

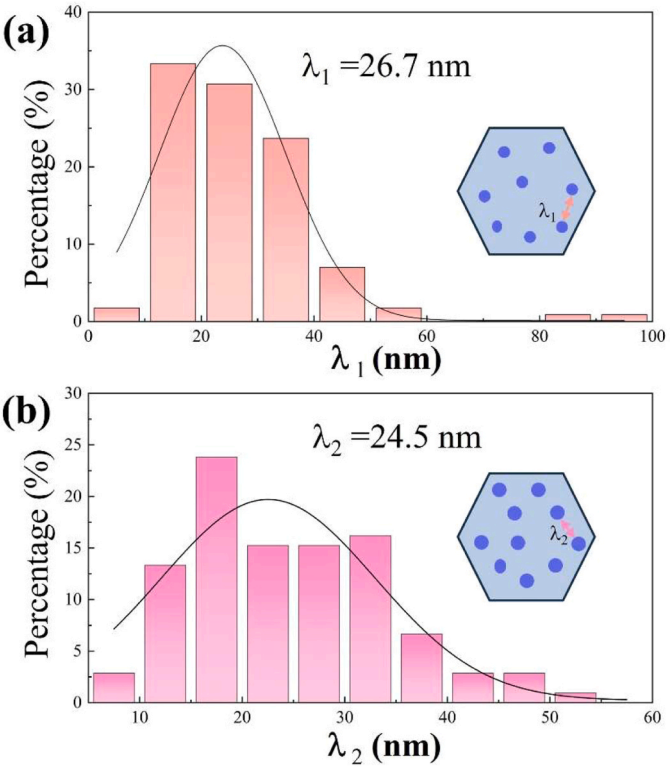

Fig. 13. Alloy precipitation phase spacing statistics: (a) Cu-0.3Zr-0.05Cr, (b) Cu-0.3Zr-0.15Cr.

statistical data are shown in Fig. 13[35].

From the above equation and the above data, the calculated value of σ_p is 388.7 MPa. The strength σ of the Cu-0.3Zr-0.15Cr alloy is $\sigma=\sigma_0+\sigma_{ds}+\sigma_p+\sigma_{GB}$=20 MPa+11.4 MPa+87.3 MPa+388.7 MPa=507.4 MPa, which is a little higher than the test value (467 MPa) and may be due to the existence of some defects within the alloy that have not been taken into account. The calculation results show that the alloy still has some internal dislocations after aging treatment and has some deformation strengthening effect. Fig. 14 shows the contribution of different strengthening mechanisms to the strength of Cu-0.3Zr-0.05Cr and Cu-0.3Zr-0.15Cr alloys. The chart shows that precipitation strengthening is the primary form of strengthening for the alloys.

4.3. Conduction mechanisms

The Cu-0.3Zr-0.15Cr alloy's resistivity is influenced by precipitated phases, grain boundaries, and dislocations. Matthiessen's rule states that the resistivity can be written as [20] :

$$\Omega = \Omega_{Cu} + \Omega_{Dis} + \Omega_{GB} + \Omega_P \tag{7}$$

The resistivity of pure Cu is represented by Ω_{Cu} in this case ($\Omega_{Cu}=1.724\times10^{-8}$ Ω•m), while the resistivity resulting from dislocations in the alloy is represented by Ω_{Dis}, which can be written as :

$$\Omega_{Dis} = \rho \bullet \Omega_{PC} \tag{8}$$

The resistivity of the dislocation brought about by Cu is represented by Ω_{PC} ($\Omega_{PC}=2\times10^{-25}$ Ω•m^3) [36]. Since ρ is the alloy's dislocation density, the resistivity in the Cu-0.3Zr-0.15Cr alloy caused by dislocations, or Ω_{Dis}, can be computed as 1.30×10^{-11} Ω•m. One can express the resistivity Ω_{GB} resulting from alloy grain boundaries as follows :

$$\Omega_{GB} = \frac{2}{3}\Omega_{Me-GB}\left(\frac{s}{v}\right) \tag{9}$$

Assuming that the grains of copper alloys are tetrahedral, Ω_{Me-GB} is the grain boundary resistivity induced by alloy ($\Omega_{Me-GB}=2.04\times10^{-16}$ Ω•m^3) [37], where s/v is the expression for the area of the grain border per unit volume. The value of s/v is assumed to be 2.37/d. The Cu-0.3Zr-0.15Cr alloy has a grain boundary resistivity of 1.86×10^{-12} Ω•m. The precipitation phase resistivity Ω_P can be written as follows:

$$\Omega_P = \Omega - \Omega_{Cu} - \Omega_{Dis} - \Omega_{GB} \tag{10}$$

Ω is the measured resistivity of the Cu-0.3Zr-0.15Cr alloy 2.04×10^{-8} Ω•m. Therefore, the Cu-0.3Zr-0.15Cr alloy's precipitated phase causes the resistivity, which is $\Omega_P=\Omega-\Omega_{Cu}-\Omega_{Dis}-\Omega_{GB}=2.04\times10^{-8}-1.72\times10^{-8}-1.30\times10^{-11}-1.86\times10^{-12}=3.2\times10^{-9}$ Ω•m.

Based on the alloy resistivity calculations, it is evident that the Cu-0.3Zr-0.15Cr alloy's copper matrix ($\Omega_{Cu}>\Omega_P>\Omega_{Dis}>\Omega_{GB}$) has the largest effect on electron hindrance, followed by the resistance resulting from the precipitated phases in the alloy. These two parts mostly dictate the alloy's resistivity. Table 2 presents the impact of distinct mechanisms on the electrical conductivity of Cu-0.3Zr-0.05Cr and Cu-0.3Zr-0.15Cr alloys.

The results of strengthening mechanism calculation show that the main strengthening methods of Cu-0.3Zr-0.05Cr alloy and Cu-0.3Zr-0.15Cr alloy after 60% of large deformation and aging treatment are deformation strengthening and precipitation strengthening. Meanwhile, Fig. 13 shows that the total contribution of solid solution strengthening, grain boundary strengthening and deformation strengthening to the strength of the two alloys is 359.5 MPa and 334.6 MPa, the former has a higher theoretical strength value. However, the strength contribution of precipitation strengthening of Cu-0.3Zr-0.15Cr alloy is 46.1 MPa higher than that of Cu-0.3Zr-0.05Cr alloy, which makes the strength of Cu-0.3Zr-0.15Cr alloy higher than that of Cu-0.3Zr-0.05Cr alloy, and thus precipitation strengthening is the main reason for the higher strength of Cu-0.3Zr-0.15Cr alloy than that of Cu-0.3Zr-0.05Cr alloy. Precipitation strengthening and softening of the alloy interact to cause the hardness change during the aging process. The alloy continuously forms a precipitation phase during the under-aging stage, improving the alloy's conductivity and hardness. At this point, precipitation strengthening and deformation strengthening predominate. As seen in Fig. 5(a) and

Table 2
Resistivity contributions of the Cu-0.3Zr-0.05Cr and Cu-0.3Zr-0.15Cr alloys.

Alloy	Ω_P, Ω•m	Ω_{Dis}, Ω•m	Ω_{GB}, Ω•m	Ω, Ω•m
Cu-0.3Zr-0.05Cr	5.9×10^{-9}	1.3×10^{-11}	7.7×10^{-12}	1.724×10^{-8}
Cu-0.3Zr-0.15Cr	3.2×10^{-9}	1.3×10^{-11}	1.8×10^{-12}	1.724×10^{-8}

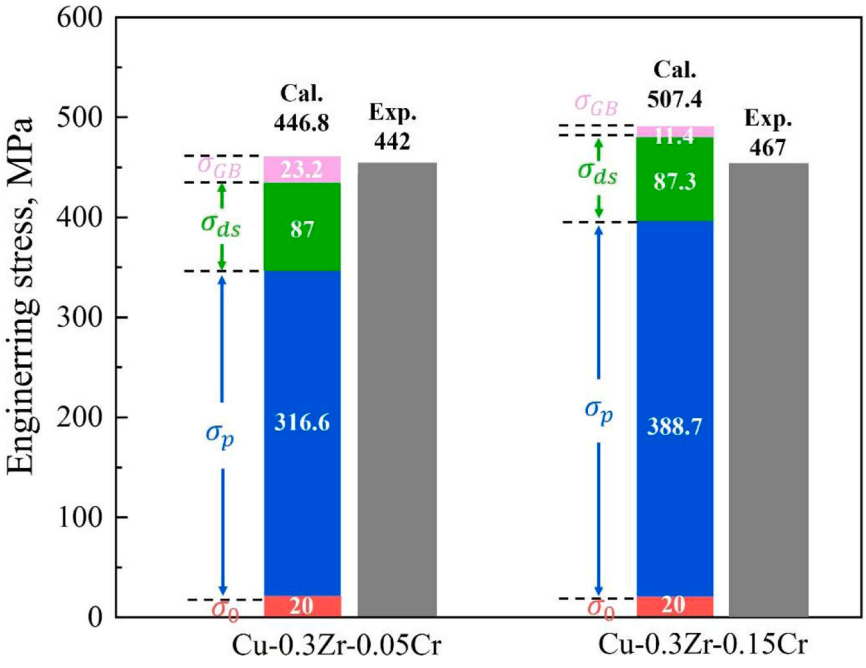

Fig. 14. Contribution of different strengthening mechanisms to strength of Cu-0.3Zr-0.05Cr and Cu-0.3Zr-0.15Cr alloys.

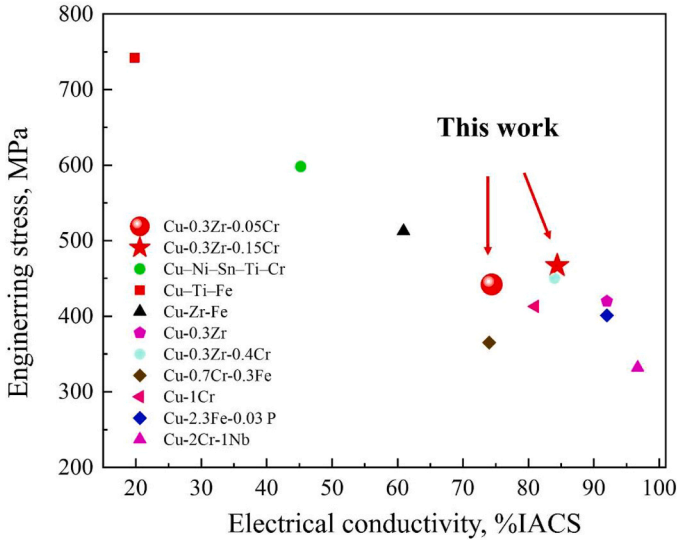

Fig. 15. Comparison of Cu-0.3Zr-0.05Cr, Cu-0.3Zr-0.15Cr, and traditional copper alloys' mechanical characteristics and electrical conductivity [20,38–40].

(c), the alloy's hardness and strength reach their maximum during the peak aging stage. During the over-aging stage, when dynamic softening becomes more prominent and the aging period is prolonged, the alloy hardness begins to decline. During this time, the conductivity continues to rise.

On the other hand, the conduction mechanism calculation indicates that the primary factors influencing the alloy's conductivity are the resistance of the copper matrix and the resistance produced by the precipitated phase. As the alloy ages, a significant number of precipitated phases precipitate in the copper matrix, effectively reducing the lattice distortion of the copper matrix and the electron scattering effect. Cu-0.3Zr-0.15Cr alloy's overall performance is enhanced due to the notable improvement in electrical conductivity resulting from this process. It can be seen from Fig. 15 that, compared with traditional copper alloys, Cu-0.3Zr-0.05Cr and Cu-0.3Zr-0.15Cr alloys have better comprehensive properties.

5. Conclusions

Cu-0.3Zr-0.05Cr and Cu-0.3Zr-0.15Cr alloys were prepared by vacuum melting, subjected to hot forging and solution treatment followed by 60% cold rolling, and aging treatment at 400 °C, 450 °C, 500 °C, and 550 °C for 0–360 min, after which their properties were examined, and the specimens were microscopically characterized, leading to the following conclusions:

(1) The alloy underwent a great refinement of the internal grain after hot forging, and the best process parameters for the Cu-0.3Zr-0.15Cr alloy were determined: 60% cold rolling followed by 450 °C aging for 120 min, resulting in 180 HV hardness, 467 MPa tensile strength, 84.4% IACS electrical conductivity, and 12.1% elongation.

(2) When the Cr content in the alloy increases from 0.05 wt% to 0.15 wt%, the Goss texture content and the maximum texture strength value of the alloy after aging increase significantly. At the same time, the alloy produces more precipitated phases during aging as the Cr content increases, leading to stronger precipitation strengthening, which makes the Cu-0.3Zr-0.15Cr alloy stronger and harder than the Cu-0.3Zr-0.05Cr alloy. Precipitation strengthening are the main strengthening mechanisms of the two alloys.

(3) A large number of fine and uniformly distributed nano-precipitated Cr and Cu_5Zr phases are formed in the aging process. The nanoscale Cr phase and the Cu matrix have a semi-coherent interface, resulting in good alloy plasticity. An abundance of precipitated phase particles improves the electrical conductivity of the Cu-0.3Zr-0.15Cr alloy by reducing distortion and electron scattering effects in the Cu matrix. This translates to an overall improvement in the alloy's performance.

CRediT authorship contribution statement

Zhengao Li: Conceptualization, Formal analysis, Methodology, Writing – original draft, Writing – review & editing. **Meng Zhou:** Project administration, Resources. **Ke Jing:** Resources, Supervision. **Yong Liu:** Resources, Supervision. **Gangao Xin:** Formal analysis. **Haoyan Hu:** Formal analysis. **Jin Zou:** Resources, Supervision. **Baohong Tian:** Resources, Supervision. **Yi Zhang:** Funding acquisition, Writing – review & editing. **Xu Li:** Investigation. **Volinsky Alex A.:** Writing – review & editing.

Declaration of Competing Interest

The authors declare that they have no known competing financial interests or personal relationships that could have appeared to influence the work reported in this paper.

Data availability

Data will be made available on request.

Acknowledgments

This work was supported by the Natural Science Foundation of China (52071134), and the Joint Foundation for Science and Technology Research and Development Plan of Henan Province (232103810030, 232103810031), the Technology Innovation Center of Graphene Metrology and Standardization for the State Market Regulation (AKYKF2309), the Program for Innovative Research Team at the University of the Henan Province (22IRTSTHN001), Key Research and Development Program of the Jiangxi Province (20224BBE51047).

References

[1] Z. Yazhou, Z. Yulin, Y. Tao, R. Xinyu, Urban green effects on land surface temperature caused by surface characteristics: a case study of summer Beijing metropolitan region, Infrared Phys. Technol. 86 (2017) 35–43, https://doi.org/10.1016/j.infrared.2017.08.008.

[2] A.K. Shukla, S.V.S. Narayana Murty, S.C. Sharma, K. Mondal, Constitutive modeling of hot deformation behavior of vacuum hot pressed Cu–8Cr–4Nb alloy, Mater. Des. 75 (2015) 57–64, https://doi.org/10.1016/j.matdes.2015.03.023.

[3] M. Gholami, J. Vesely, I. Altenberger, H.-A. Kuhn, M. Janecek, M. Wollmann, L. Wagner, Effects of microstructure on mechanical properties of CuNiSi alloys, J. Alloy. Compd. 696 (2017) 201–212, https://doi.org/10.1016/j.jallcom.2016.11.233.

[4] Kazuhiko Fukamachi, Masahiro Kimura, Age-hardening structure and mechanism of Cu–3at%Ni–1.5 at%Si Corson alloy, Mater. Sci. Eng. A 831 (2022) 142220, https://doi.org/10.1016/j.msea.2021.142220.

[5] Z. Wang, J. Li, Z. Fan, Y. Zhang, S. Hui, L. Peng, G. Huang, H. Xie, X. Mi, Effects of Co addition on the microstructure and properties of elastic Cu-Ni-Si-based alloys for electrical connectors, Materials 14 (8) (2021) 1996, https://doi.org/10.3390/ma14081996.

[6] Anoop R. Kini, Dora Maischner, Andreas Weisheit, Dirk Ponge, Baptiste Gault, Eric A. Jägle, Dierk Raabe, In-situ synthesis via laser metal deposition of a lean Cu–3.4Cr–0.6Nb (at%) conductive alloy hardened by Cr nano-scale precipitates and by Laves phase micro-particles, Acta Mater. 197 (2020) 330–340, https://doi.org/10.1016/j.actamat.2020.07.035.

[7] Y. Zhang, H.L. Sun, A.A. Volinsky, et al., Characterization of the hot deformation behavior of Cu–Cr–Zr alloy by processing maps, Acta Metall. Sin. (Engl. Lett.) 29 (2016) 422–430, https://doi.org/10.1007/s40195-016-0404-3.

[8] Wang Junfeng, Chen Jinshui, Guo Chengjun, Zhang Jianbo, Xiao Xiangpeng, Yang Bin, Effect of heat treatment on low cycle fatigue properties of Cu–Cr–Zr alloy, Mater. Charact. 158 (2019) 109940, https://doi.org/10.1016/j.matchar.2019.109940.

[9] Jinshui Chen, Junfeng Wang, Xiangpeng Xiao, Hang Wang, Huiming Chen, Bin Yang, Contribution of Zr to strength and grain refinement in CuCrZr alloy, Mater. Sci. Eng. A 756 (2019) 464–473, https://doi.org/10.1016/j.msea.2019.04.053.
[10] Muzhi Ma, Zhou Li, Zhu Xiao, Hanrui Zhu, Xi Zhang, Fenyan Zhao, Microstructure and properties of a novel Cu-Cr-Yb alloy with high strength, high electrical conductivity and good softening resistance, Mater. Sci. Eng. A 795 (2020) 140001, https://doi.org/10.1016/j.msea.2020.140001.
[11] Kuo Yang, Yihan Wang, Mingxing Guo, Hu Wang, Yongda Mo, Xueguang Dong, Huafen Lou, Recent development of advanced precipitation-strengthened Cu alloys with high strength and conductivity: a review, Prog. Mater. Sci. 138 (2023) 101141, https://doi.org/10.1016/j.pmatsci.2023.101141.
[12] Shuo Ma, Qing Zhang, Jiantao Fan, Liming Fu, Mao Wen, Manping Liu, Aidang Shan, Excellent combination of strength, conductivity and ductility realized in a dilute Cu-Cr-Zr alloy by coherent nanoprecipitates, Mater. Sci. Eng. A 885 (2023) 145614, https://doi.org/10.1016/j.msea.2023.145614.
[13] Huadong Fu, Sheng Xu, Wei Li, Jianxin Xie, Hongbin Zhao, Zhijun Pan, Effect of rolling and aging processes on microstructure and properties of Cu-Cr-Zr alloy, Mater. Sci. Eng. A 700 (2017) 107–115, https://doi.org/10.1016/j.msea.2017.05.114.
[14] A. Bodyakova, R. Mishnev, A. Belyakov, et al., Effect of chromium content on precipitation in Cu–Cr–Zr alloys, J. Mater. Sci. Technol. 57 (2022) 13043–13059, https://doi.org/10.1007/s10853-022-07454-8.
[15] Gui Kuang, Kesong Miao, Xuewen Li, Hao Wu, Chenglu Liu, Rengeng Li, Guohua Fan, In-situ observation of microstructure and orientation evolution of the Cu–Cr–Zr-Hf alloys, Mater. Sci. Eng. A 865 (2023) 144642, https://doi.org/10.1016/j.msea.2023.144642.
[16] C.Z. Xu, Q.J. Wang, M.S. Zheng, J.W. Zhu, J.D. Li, M.Q. Huang, Q.M. Jia, Z.Z. Du, Microstructure and properties of ultra-fine grain Cu–Cr alloy prepared by equal-channel angular pressing, Mater. Sci. Eng. A 459 (Issues 1–2) (2007) 303–308, https://doi.org/10.1016/j.msea.2007.01.105.
[17] Kun Xia Wei, Wei Wei, Fei Wang, Qing Bo Du, Igor V. Alexandrov, Jing Hu, Microstructure, mechanical properties and electrical conductivity of industrial Cu–0.5%Cr alloy processed by severe plastic deformation, Mater. Sci. Eng. A 528 (2011) 1478–1484, https://doi.org/10.1016/j.msea.2010.10.059.
[18] Naoki Takata, Yusuke Ohtake, Kazuhisa Kita, Kazuo Kitagawa, Nobuhiro Tsuji, Increasing the ductility of ultrafine-grained copper alloy by introducing fine precipitates, Scr. Mater. 60 (2009) 590–593, https://doi.org/10.1016/j.scriptamat.2008.12.018.
[19] I. Shakhova, Z. Yanushkevich, I. Fedorova, A. Belyakov, R. Kaibyshev, Grain refinement in a Cu–Cr–Zr alloy during multidirectional forging, Mater. Sci. Eng. A 606 (2014) 380–389, https://doi.org/10.1016/j.msea.2014.03.116.
[20] Shunlong Tang, Meng Zhou, Yi Zhang, Deye Xu, Zhiyang Zhang, Xianhua Zheng, De Li, Xu Li, Baohong Tian, Yanlin Jia, Yong Liu, Alex A. Volinsky, Ekaterina S. Marchenko, Improved microstructure, mechanical properties and electrical conductivity of the Cu–Ni–Sn–Ti–Cr alloy due to Ce micro-addition, Mater. Sci. Eng. A 871 (2023) 144910, https://doi.org/10.1016/j.msea.2023.144910.
[21] Yanhui Dong, Dan Zhang, Daguang Li, Heng Jia, Weiping Qin, Control of Ostwald ripening, Sci. China Mater. 66 (2023) 1249–1255, https://doi.org/10.1007/s40843-022-2233-3.
[22] Li Hai, Xu Wei, Wang Zhixiu, Fang Bijun, Song Renguo, Zheng Ziqiao, Ostwald Ripening Behavior of Al_8CeCu_4 Phase in Al-14Cu-7Ce Alloy, ISSN 1875-5372, Rare Met. Mater. Eng. Volume 45 (Issue 5) (2016) 1106–1110, https://doi.org/10.1016/S1875-5372(16)30102-3.
[23] A. Elasheri, E.M. Elgallad, N. Parson, et al., Improving the dispersoid distribution and recrystallization resistance of a Zr-containing 6xxx alloy using two-step homogenization, Philos. Mag. 102 (2022) 2345–2361, https://doi.org/10.1080/14786435.2022.2103597.
[24] Atanu Chaudhuri, Ananta N. Behera, Apu Sarkar, Rajeev Kapoor, Ranjit K. Ray, Satyam Suwas, Hot deformation behaviour of Mo-TZM and understanding the restoration processes involved, Acta Mater. 164 (2019) 153–164, https://doi.org/10.1016/j.actamat.2018.10.037.
[25] Yongfeng Geng, Yijie Ban, Bingjie Wang, Xu Li, Kexing Song, Yi Zhang, Yanlin Jia, Baohong Tian, Yong Liu, Alex A. Volinsky, A review of microstructure and texture evolution with nanoscale precipitates for copper alloys, J. Mater. Res. Technol. 9 (2020) 11918–11934, https://doi.org/10.1016/j.jmrt.2020.08.055.
[26] S. Nagarjuna, M. Srinivas, Elevated temperature tensile behaviour of a Cu–4.5Ti alloy, Mater. Sci. Eng. A 406 (2005) 186–194, https://doi.org/10.1016/j.msea.2005.06.064.
[27] Yanlin Jia, Yong Pang, Jiang Yi, Qian Lei, Zhou Li, Zhu Xiao, Effects of pre-aging on microstructure and properties of Cu-Ni-Si alloys, J. Alloy. Compd. 942 (2023) 169033, https://doi.org/10.1016/j.jallcom.2023.169033.
[28] S. Nagarjuna, K. Balasubramanian, D.S. Sarma, Effect of prior cold work on mechanical properties, electrical conductivity and microstructure of aged Cu-Ti alloys, J. Mater. Sci. 34 (1999) 2929–2942, https://doi.org/10.1023/A:1004603906359.
[29] Weijiang Liu, Jian Li, Xin Chen, Minghua Ji, Xiangpeng Xiao, Hang Wang, Bin Yang, Effect of vanadium on the microstructure and kinetics of discontinuous precipitation in Cu–3.2Ti–0.2Fe alloy, J. Mater. Res. Technol. 14 (2021) 121–136, https://doi.org/10.1016/j.jmrt.2021.06.045.
[30] Yongfeng Geng, Yijie Ban, Xu Li, Yi Zhang, Yanlin Jia, Baohong Tian, Meng Zhou, Yong Liu, Alex A. Volinsky, Kexing Song, Shunlong Tang, Excellent mechanical properties and high electrical conductivity of Cu-Co-Si-Ti alloy due to multiple strengthening, Mater. Sci. Eng. A 821 (2021) 141639, https://doi.org/10.1016/j.msea.2021.141639.
[31] J.Y. He, H. Wang, H.L. Huang, X.D. Xu, M.W. Chen, Y. Wu, X.J. Liu, T.G. Nieh, K. An, Z.P. Lu, A precipitation-hardened high-entropy alloy with outstanding tensile properties, Acta Mater. 102 (2016) 187–196, https://doi.org/10.1016/j.actamat.2015.08.076.
[32] Niels Hansen, Hall–Petch relation and boundary strengthening, Scr. Mater. 51 (2004) 801–806, https://doi.org/10.1016/j.scriptamat.2004.06.002.
[33] Z. Wang, W. Lu, H. Zhao, C.H. Liebscher, J. He, D. Ponge, D. Raabe, Z. Li, Ultrastrong lightweight compositionally complex steels via dual-nanoprecipitation, Sci. Adv. 6 (46) (2020) eaba9543, https://doi.org/10.1126/sciadv.aba9543.
[34] Yake Wu, Ya Li, Junyong Lu, Sai Tan, Feng Jiang, Jun Sun, Correlations between microstructures and properties of Cu-Ni-Si-Cr alloy, Mater. Sci. Eng. A 731 (2018) 403–412, https://doi.org/10.1016/j.msea.2018.06.075.
[35] K. JING, R. LIU, Z.M. XIE, et al., Excellent high-temperature strength and ductility of the ZrC nanoparticles dispersed molybdenum, Acta Mater. 227 (2022) 1359–6454, https://doi.org/10.1016/j.actamat.2022.117725.
[36] Wei Zeng, Jingwen Xie, Dengshan Zhou, Zhiqiang Fu, Deliang Zhang, Enrique J. Lavernia, Bulk Cu-NbC nanocomposites with high strength and high electrical conductivity, J. Alloy. Compd. 745 (2018) 55–62, https://doi.org/10.1016/j.jallcom.2018.02.215.
[37] Yijie Ban, Yongfeng Geng, Jinrui Hou, Yi Zhang, Meng Zhou, Yanlin Jia, Baohong Tian, Yong Liu, Xu Li, Alex A. Volinsky, Properties and precipitates of the high strength and electrical conductivity Cu-Ni-Co-Si-Cr alloy, J. Mater. Sci. Technol. 93 (2021) 1–6, https://doi.org/10.1016/j.jmst.2021.03.049.
[38] Gang'ao Xin, Meng Zhou, Ke Jing, Haoyan Hu, Zheng'ao Li, Yi Zhang, Qian Bai, Caijiao Tian, Baohong Tian, Xu Li, Alex A. Volinsky, Jin Zou, Heat treatment effects on microstructure and properties of Cu–Ti–Fe alloys, Mater. Sci. Eng. A 892 (2024) 146068, https://doi.org/10.1016/j.msea.2023.146068.
[39] Mixue Guo, Meng Zhou, Jin Zou, Ke Jing, Haoyan Hu, Yi Zhang, Qian Bai, Caijiao Tian, Baohong Tian, Xu Li, Alex A. Volinsky, Y effects on the Cu-Zr-Fe alloys' aging behavior and properties, J. Alloy. Compd. 977 (2024), https://doi.org/10.1016/j.jallcom.2024.173418.
[40] Y.K. Ren, X.Q. Lü, Z.M. Liu, B. Wei, T. Lei, Q. Li, X.B. Ji, W.T. Deng, Y.K. Ai, Microstructure and properties of Cu-2Cr-1Nb alloy fabricated by spark plasma sintering, Trans. Nonferrous Met. Soc. 32 (2022) 2276–2289, https://doi.org/10.1016/ S1003-6326(22)65947-8.